machines

MDPI

Article

Robust Driving Control Design for Precise Positional Motions of Permanent Magnet Synchronous Motor Driven Rotary Machines with Position-Dependent Periodic Disturbances

Syh-Shiuh Yeh [1,*] and Zhi-Hong Liu [2]

[1] Department of Mechanical Engineering, National Taipei University of Technology, Taipei 10608, Taiwan
[2] Institute of Mechatronic Engineering, National Taipei University of Technology, Taipei 10608, Taiwan; t108408080@ntut.edu.tw
* Correspondence: ssyeh@ntut.edu.tw

Abstract: Position-dependent periodic disturbances often limit the accuracy and smoothness of the positional motion of permanent magnet synchronous motor (PMSM)-driven rotary machines. Because the period of these disturbances varies with the motion velocity of the rotary machine, spatial domain control methods such as spatial iterative learning control (SILC) and spatial repetitive control (SRC) have been proposed and applied to improve rotary machine motion control designs. However, problems with learning period convergence and rotary machine dynamics significantly affect transient motion, further constraining the overall motion performance. To address these challenges, this study developed a robust driving control (RDC) that integrates a robust control design with position-dependent periodic disturbance feedforward compensation, rotary machine dynamics compensation, and proportional–proportional integral feedback control. A position-dependent periodic disturbance model was developed using multiple position–sinusoidal signals and identified using a spatial fast Fourier transform. RDC compensates for disturbances and dynamics and considers the effects of model parameter uncertainty and modeling error on the stability of the control system. Several motion control experiments were conducted on a PMSM test bench to compare the RDC, SILC, and SRC. The experimental results demonstrated that although both SILC and SRC can effectively suppress position-dependent periodic disturbances, SILC provides slower position error convergence owing to the learning process, and SILC and SRC result in significant position errors because of the influence of the PMSM-driven rotary machine dynamics. RDC not only suppresses position-dependent periodic disturbances, but also significantly reduces position errors with a reduction rate of 90%. Therefore, the RDC developed in this study effectively suppressed position-dependent periodic disturbances and significantly improved both the transient-state and steady-state position-tracking performances of the PMSM-driven rotary machine.

Keywords: robust driving control; precise positional motion; permanent magnet synchronous motor; rotary machine; position-dependent periodic disturbance

Citation: Yeh, S.-S.; Liu, Z.-H. Robust Driving Control Design for Precise Positional Motions of Permanent Magnet Synchronous Motor Driven Rotary Machines with Position-Dependent Periodic Disturbances. *Machines* **2024**, *12*, 771. https://doi.org/10.3390/machines12110771

Academic Editor: Juan Carlos Travieso-Torres

Received: 25 September 2024
Revised: 21 October 2024
Accepted: 30 October 2024
Published: 1 November 2024

1. Introduction

Rotary machines are widely utilized in various industrial applications, where high motion accuracy and smoothness are often critical. However, the motions of these machines are frequently affected by external disturbances. Many of these disturbances exhibit position periodicity; that is, they exhibit periodic changes based on the rotating angular position, causing the disturbance period to vary with the motion velocity of the rotary machine [1–3]. In a permanent magnet synchronous motor (PMSM)-driven rotary machine, electromagnetic and cogging torque ripples introduce position periodicity, with the period closely related to the PMSM design [4]. Additionally, the position-dependent friction torque in a PMSM and rotary machine contributes to the position periodicity, which is linked to the friction characteristics of the mechanical interface [5,6]. External forces on rotary machines

also generate position-periodic disturbances [7–10]. Therefore, addressing the impact of position-dependent periodic disturbances to enhance the accuracy and smoothness is a critical challenge in the motion control design of PMSM-driven rotary machines.

Disturbance estimation and compensation are commonly employed in the motion control of PMSM-driven rotary machines because of their straightforward implementation and effectiveness in mitigating the adverse effects of external disturbance [11–15]. Although these methods can effectively suppress the adverse impacts of constant or slowly changing disturbances on the motion of a rotary machine, they cannot effectively suppress position-dependent periodic disturbances. Because these disturbances are periodic, their periods change with the motion velocity of the rotary machine. Therefore, estimating and compensating for position-dependent periodic disturbances is essential for effective motion control. Because such disturbances produce repetitive effects, iterative learning control (ILC) and repetitive control (RC) have proven to be effective in mitigating their impact and improving the performance of rotary machines.

When a PMSM-driven rotary machine performs repeated motion and encounters repetitive external disturbances, ILC can effectively mitigate the influence of these disturbances and enhance the motion performance. Liu et al. [16] developed a robust ILC approach for PMSM drives, utilizing the ILC law to suppress periodic torque ripples by learning the state-dependent function and incorporating an adaptive sliding mode control law to enhance the disturbance robustness. Huo et al. [17] introduced a data-driven ILC method with a data-based learning gain design to address the spatial periodic disturbances in a PMSM-driven turntable by projecting error signals onto the subspace spanned by the plant and disturbance models. Mohammed et al. [18] proposed an improved ILC that integrates ILC with a feedback linearization control scheme to reduce periodic disturbances and enhance the speed-tracking performance in a surface-mounted PMSM. Although ILC can significantly improve the repeated motion performance of a PMSM-driven rotary machine, it requires relearning when the motion conditions change. Its motion velocity can alter the disturbance period of the position-dependent periodic disturbances. Thus, a new learning process is required for the ILC to maintain its effectiveness. In other words, when the motion velocity of a PMSM-driven rotary machine changes, the temporal ILC must undergo a new learning process to remain effective; otherwise, it will not improve the motion performance. Therefore, spatial ILC (SILC) has been proposed to enhance the motion performance of PMSM-driven rotary machines and address the spatial domain repeatability of position-dependent periodic disturbances. To address the challenge of periodic current ripples in PMSMs, Lei et al. [19] developed an enhanced deadbeat predictive current control that integrates a sliding-mode observer with ILC with a spatial learning ability. Wang et al. [20] introduced a model predictive control approach that employs position-dependent ILC to estimate and compensate for periodic disturbances in the spatial domain when arc motors operate at various speeds. Although both temporal and spatial ILC can improve the motion performance of PMSM-driven rotary machines, they often require extensive data recording and processing. This increases the computational burden on the control system. Moreover, SILC involves a lengthy iterative learning process, which can limit the overall improvement in motion performance.

RC is a control method based on the internal model principle and effectively mitigates the adverse effects of periodic disturbances under steady-state conditions. Thus, it enhances the tracking performance of a control system [21,22]. RC is employed to manage periodic disturbances in PMSM-driven rotary machines, reducing the tracking errors at the fundamental and harmonic frequencies of the disturbances. Mahawan and Luo [23] improved the conventional RC scheme using operator theory to map a time function into an alternative monotone function. This enabled the modified repetitive controller to track time-varying periodic references accurately. To address periodic disturbances with uncertain periods in the radial tracking control of a compact disc player, Steinbuch [24] developed a robust RC that incorporates multiple memory loops to suppress disturbances with small period-time variations. Steinbuch et al. [25] subsequently advanced this approach by developing

a high-order RC with a linear programming algorithm to balance the robustness of the period-time change and the error spectrum reduction. Kalyanam and Tsao [26] introduced a two-period plug-in RC, including stability and sensitivity analyses, to suppress dual-periodic disturbances in the servo control of a hard disk drive. Cui et al. [27] combined a frequency-adaptive dual-mode repetitive controller with a phase-shift notch filter to create a hybrid fractional RC that addresses the harmonic current caused by mass imbalance and sensor runout in magnetically suspended rotor systems. Blanken et al. [28] developed a sequential design approach for multiple repetitive controllers in a cascaded structure to mitigate multiple periodic disturbances, thereby achieving fast convergence and precise tracking performance.

Although RC effectively suppresses periodic disturbances and improves the tracking performance in the motion of PMSM-driven rotary machines, it relies on two fundamental assumptions: external disturbances must be periodic, and the control system must be asymptotically stable before integrating RC [29]. Because the period of position-dependent periodic disturbances varies with changes in motion velocity, temporal RC is often used for the constant-velocity motion control of PMSM-driven rotary machines, and the tracking control performance is frequently limited for motions with varying velocities. Moreover, although robust RC has been proposed to address varying and multiple periodic disturbances, its performance is constrained by the range of motion velocities and changes in the external disturbance periods. Spatial RC (SRC) has been proposed to improve the motion tracking performance based on the spatial domain repeatability of position-dependent disturbances. Mooren et al. [1] developed an SRC that uses Gaussian processes to model and identify spatial disturbances. The obtained model was applied to design a Gaussian-process-based RC to compensate for spatial periodic disturbances in a substrate carrier system. By deriving and analyzing a spatial internal model with spatially periodic signals, Huo et al. [3] developed an SRC design incorporating a spatial low-pass filter and a frequency alignment method to suppress position-dependent periodic disturbances and enhance position-tracking performance in a dual-axis turntable. Liu et al. [2] developed a cycle-aligned RC based on a spatial internal model. They used data-storage techniques to accurately suppress spatial disturbances in a dual-axis turntable with a spatial auxiliary stabilizing compensator, spatial low-pass compensator, and time-advance element. Wu et al. [30] introduced a position-based RC torque observer to address the cogging-torque problem in PMSMs through cogging-torque estimation and feedforward compensation, either online or offline. Castro et al. [31] developed an SRC design and a robust synthesis procedure to manage position-dependent periodic signals in a direct-current motor, ensuring stability and performance. Although SRC effectively suppresses the adverse effects of position-dependent periodic disturbances under steady-state conditions, transient motion in PMSM-driven rotary machines remains significantly affected by these disturbances. The duration of this effect depends on the disturbance period and machine motion velocity. Additionally, SRC often suppresses position-dependent disturbances but may not mitigate the impact of the dynamic characteristics of the PMSM-driven rotary machine on motion tracking performance or address the problems of parameter uncertainty and modeling errors on the stability of motion control systems. To mitigate the adverse effects of position-dependent periodic disturbances and enhance the tracking performance of the positional motion in PMSM-driven rotary machines, this study developed robust driving control (RDC) for PMSMs.

This study began by modeling and identifying the position-dependent periodic disturbances in PMSM-driven rotary machines. The angular position and driving torque signals of the PMSM-driven rotary machine were obtained during the low-velocity motion experiments. These signals were analyzed using spatial fast Fourier transform (FFT) to determine the position-dependent periodic disturbance parameters, such as the number, magnitude, frequency, and phase of the main disturbance components. A position-dependent periodic disturbance model was then created using multiple position-sinusoidal signals for feedforward compensation. This study employed a robust control method to design the

PMSM RDC. Based on the widely used proportional–proportional integral (P-PI) feedback control structure in commercial PMSM drives, a position-dependent periodic disturbance model was integrated into the P-PI feedback control, and the RDC was designed considering the parameter uncertainty and modeling errors of the position-dependent periodic disturbance model and the PMSM-driven rotary machine dynamic model. Motion control experiments were conducted using a PMSM test bench to evaluate and validate the feasibility and performance of the RDC. These experiments assessed the effectiveness of transient-state and steady-state conditions across various motion velocities. Additionally, this study compared RDC with SILC and SRC, both of which were implemented using the P-PI feedback control structure. The experimental results indicated that SILC, SRC, and RDC effectively mitigated the adverse effects of position-dependent periodic disturbances on PMSM motion. However, compared with RDC, both SILC and SRC resulted in larger position errors owing to the impact of the dynamic characteristics of the PMSM-driven rotary machine. Therefore, the experimental results indicated that the RDC developed in this study effectively suppresses the adverse effects of position-dependent periodic disturbances on a PMSM-driven rotary machine and significantly enhances the tracking performance of its positional motion.

The remainder of this paper is organized as follows. Section 2 describes the preliminary work, including the dynamics of the PMSM-driven rotary machine, P-PI feedback-and-compensation control structure, and designs of the SILC and SRC based on the P-PI feedback control structure. Section 3 describes the RDC developed in this study, including the control design approach, stability analysis, and control parameter design. Section 4 presents the motion control experimental results of the PMSM test bench and compares the motion performance of RDC with those of the two spatial domain control designs. Finally, Section 5 concludes the paper.

2. Preliminary Work

2.1. Dynamics of a PMSM-Driven Rotary Machine

The dynamic equation of a PMSM-driven rotary machine is given by Equation (1):

$$\tau_m = J_m\ddot{\theta}_m + B_m\dot{\theta}_m + \tau_m^{sc} + \sum_{i=1}^{N}(L_i \sin(\omega_i\theta_m + \varphi_i)) \quad (1)$$

where τ_m denotes the driving torque of the PMSM; J_m and B_m represent the equivalent moment of inertia and equivalent viscous friction coefficient of the PMSM, respectively; θ_m denotes the actual angular position of the PMSM; τ_m^{sc} denotes the compound friction torque comprising the Coulomb and static friction torques; and N, L_i, ω_i, and φ_i denote the number of main components of the position-dependent periodic disturbance, magnitude, frequency, and phase of the ith main component, respectively. The equivalent moment of inertia J_m can be determined through an experiment to estimate the moment of inertia [32]. The equivalent viscous friction coefficient B_m and compound friction torque τ_m^{sc} can be determined via a constant-speed experiment [32]. The compound friction torque τ_m^{sc} is given by Equation (2):

$$\tau_m^{sc} = \left[\tau_m^c + (\tau_m^s - \tau_m^c)e^{-(|\frac{\dot{\theta}_m}{\dot{\theta}_m^s}|)^{\delta}}\right]\mathrm{sgn}\left(\dot{\theta}_m\right) \quad (2)$$

where τ_m^c denotes the Coulomb friction torque, τ_m^s the static friction torque, $\dot{\theta}_m^s$ the Stribeck velocity, and δ the Stribeck shape factor. The position-dependent periodic disturbance parameters N, L_i, ω_i, and φ_i can be determined through the spatial FFT of the PMSM driving torque signal and actual angular position signal obtained from low-velocity motion experiments [5].

2.2. P-PI Feedback-and-Compensation Control Design

The structure of P-PI feedback control, which is widely used in commercial PMSM drives, is shown in Figure 1a, where the position feedback control uses proportional control, the velocity feedback control uses proportional integral control, and both feedback controls adopt a cascade control structure. k_{pp} denotes the proportional control parameter. $k_{vp}\left(1+\frac{1}{T_i s}\right)$ denotes the transfer function of the PI controller, and k_{vp} and T_i denote the proportional and integral control parameters, respectively. K_i denotes the torque constant, θ_m^r the angular position command of the PMSM, and $\dot{\theta}_m$ the actual angular velocity of the PMSM. Although the P-PI feedback control structure shown in Figure 1a is effective and easy to implement, a P-PI feedback-and-compensation control structure has been proposed to improve the motion performance of the PMSM through control-signal compensation without excessively increasing the computational burden of PMSM drives [33], as shown in Figure 1b. Here, Θ_m^a, Ω_m^a, and I_m^a denote the position, velocity, and current compensation, respectively. The PMSM driving torque τ_m of the P-PI feedback-and-compensation control structure is represented by Equation (3):

$$\tau_m = K_i G k_{pp}(\theta_m^r - \theta_m) - K_i G\dot{\theta}_m + K_i G k_{pp}\Theta_m^a + K_i G\Omega_m^a + K_i I_m^a \tag{3}$$

where G is the transfer function of the PI controller. This study adopted the common control-parameter-adjustment rule for commercial PMSM drives to achieve the following:

- To adjust the velocity feedback proportional control parameter k_{vp} and integral control parameter T_i to ensure the velocity response of the PMSM has a short rise time with no significant overshoot.
- To adjust the position feedback proportional control parameter k_{pp} to ensure that the position response of the PMSM has a short rise time with no overshoot.

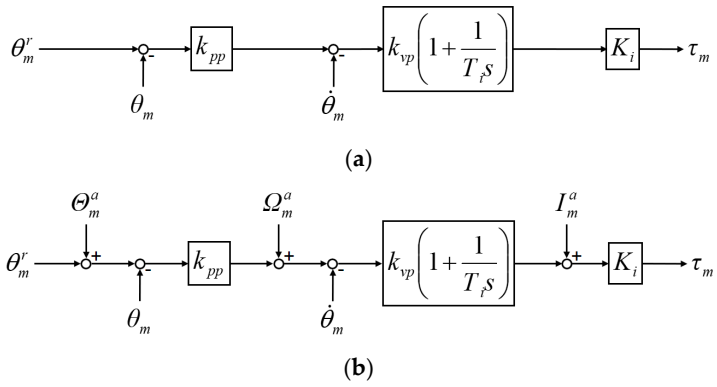

Figure 1. P-PI feedback control and compensation: (**a**) P-PI feedback control structure. (**b**) P-PI feedback-and-compensation control structure [33].

2.3. SILC Design

SILC is an extension of temporal ILC. In this study, SILC was applied to the P-PI control structure, as shown in Figure 2. Here, the SILC design refers to the PI-ILC scheme [16] and is applied to the velocity feedback control of the P-PI control structure [34]. $\dot{\theta}_m^r$ denotes the PMSM angular velocity command. T_t^θ and T_θ^t use data storage and interpolation techniques to convert the signal from the temporal domain to the spatial domain and from the spatial domain to the temporal domain, respectively [35]. The ILC law uses a proportional-type ILC as expressed in Equation (4):

$$\Omega_m^a(\theta)_k = \Omega_m^a(\theta)_{k-1} + k_{ILCp}\varepsilon(\theta)_k \tag{4}$$

where $\Omega_m^a(\theta)_k$ and $\Omega_m^a(\theta)_{k-1}$ denote the spatial domain velocity compensation of No. (k) and No. $(k-1)$ iterations, respectively; $\varepsilon(\theta)_k$ denotes the spatial domain velocity error of

the No. (k) iteration; and k_{ILCp} denotes the proportional parameter of the ILC. The velocity error must be converted from the temporal domain to the spatial domain by T_t^θ, and the velocity compensation must be converted from the spatial domain to the temporal domain through T_θ^t. For the control structure shown in Figure 2, the control parameters are adjusted as follows:

- Before applying SILC, the velocity feedback and position feedback control parameters are adjusted using the common control-parameter-adjustment rule mentioned in Section 2.2.
- SILC is applied, and the proportional parameter k_{ILCp} is adjusted according to Equation (4) for the PMSM to achieve a lower position error root-mean-square value and rapid convergence speed.

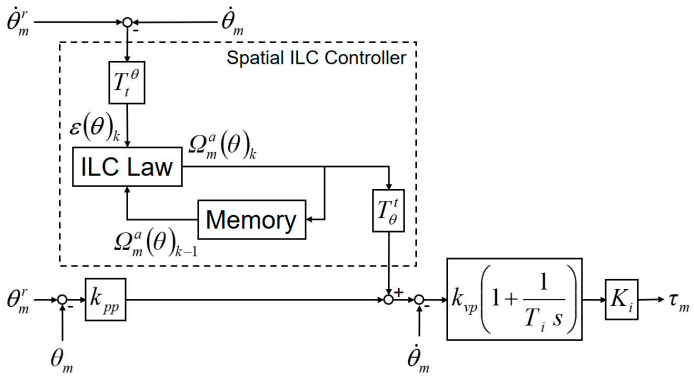

Figure 2. SILC design based on P-PI feedback control structure.

2.4. SRC Design

SRC is an extension of temporal RC. Given that the P-PI feedback control structure is widely used in commercial PMSM drives, this study integrated SRC into the P-PI feedback control structure, as shown in Figure 3. Here, p represents the spatial Laplace transform operator, λ enotes the spatial disturbance period, $e^{-\lambda p}$ is the spatial delay term, and $Q(s)$ is a low-pass filter. The spatial delay term $e^{-\lambda p}$ can be approximated using storage and interpolation techniques [35], and the spatial disturbance period λ must be adjusted to mitigate the frequency bias introduced by the low-pass filter [3]. The low-pass filter $Q(s)$ is expressed in Equation (5) [3]:

$$Q(s) = \frac{\left(\Omega_{sc}{}^2\right)\left(\dot{\theta}_m{}^2\right)}{s^2 + \sqrt{2}(\Omega_{sc})\left(\dot{\theta}_m\right)s + \left(\Omega_{sc}{}^2\right)\left(\dot{\theta}_m{}^2\right)} \tag{5}$$

where Ω_{sc} denotes the spatial cutoff angular frequency. For the control structure presented in Figure 3, the control parameters are adjusted as follows:

- The spatial frequency of the position-dependent periodic disturbance of the PMSM-driven rotary machine is identified.
- Before SRC is applied, the velocity-feedback and position-feedback control parameters are adjusted using the common control-parameter-adjustment rule mentioned in Section 2.2.
- SRC is applied, and a low-pass filter is designed according to Equation (5).
- The spatial disturbance period λ of the spatial delay term is adjusted according to the identified spatial frequency of the position-dependent periodic disturbance to further mitigate the adverse effects.

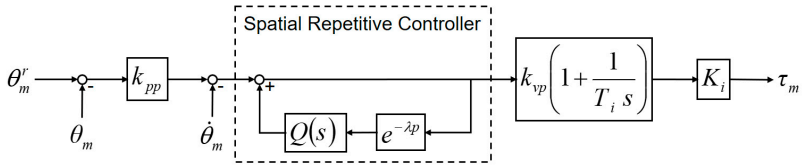

Figure 3. SRC design based on the P-PI feedback control structure.

3. RDC Design

Considering the dynamic equation of the PMSM-driven rotary machine given by Equation (1), this study referred to the P-PI feedback-and-compensation control structure depicted in Figure 1b and designed the velocity and current compensation of the RDC, as expressed in Equations (6) and (7), respectively:

$$\Omega_m^a = \dot{\theta}_m^r \tag{6}$$

$$I_m^a = \frac{1}{K_i}\left(\hat{J}_m\ddot{\theta}_m^r + \hat{B}_m\dot{\theta}_m^r + \hat{\tau}_m^{sc} + \sum_{i=1}^{n}\left(\hat{L}_i\sin(\hat{\omega}_i\theta_m^r + \hat{\varphi}_i)\right) + \delta\tau_m\right) \tag{7}$$

where $\hat{J}_m$ is the estimated equivalent moment of inertia; $\hat{B}_m$ is the estimated equivalent viscous friction coefficient; $\hat{\tau}_m^{sc}$ is the estimated compound friction torque; $\delta\tau_m$ is an additional compensation term designed to mitigate the influence of model parameter uncertainty and modeling errors; and n, $\hat{L}_i$, $\hat{\omega}_i$, and $\hat{\varphi}_i$ are the estimated number, magnitude, frequency, and phase of the ith main component, respectively. $\ddot{\theta}_m^r$ denotes the PMSM angular acceleration command.

By substituting Equations (6) and (7) into Equation (3) and letting $\Theta_m^a = 0$, the PMSM driving torque τ_m can be rewritten as Equation (8):

$$\tau_m = \begin{pmatrix} K_iGk_{pp}(\theta_m^r - \theta_m) - K_iG\dot{\theta}_m + K_iG\dot{\theta}_m^r \\ +\hat{J}_m\ddot{\theta}_m^r + \hat{B}_m\dot{\theta}_m^r + \hat{\tau}_m^{sc} + \sum\limits_{i=1}^{n}\left(\hat{L}_i\sin(\hat{\omega}_i\theta_m^r + \hat{\varphi}_i)\right) + \delta\tau_m \end{pmatrix} \tag{8}$$

By substituting Equation (8) into Equation (1), the dynamic equation of the PMSM-driven rotary machine can be rewritten as Equations (9) and (10):

$$J_m\ddot{\theta}_m = \begin{pmatrix} K_iGk_{pp}(\theta_m^r - \theta_m) - K_iG\dot{\theta}_m + K_iG\dot{\theta}_m^r \\ +\hat{J}_m\ddot{\theta}_m^r + \hat{B}_m\dot{\theta}_m^r + \hat{\tau}_m^{sc} + \sum\limits_{i=1}^{n}\left(\hat{L}_i\sin(\hat{\omega}_i\theta_m^r + \hat{\varphi}_i)\right) + \delta\tau_m \\ -B_m\dot{\theta}_m - \tau_m^{sc} - \sum\limits_{i=1}^{N}\left(L_i\sin(\omega_i\theta_m + \varphi_i)\right) \end{pmatrix} \tag{9}$$

$$J_m\ddot{\theta}_m = \begin{pmatrix} K_iGk_{pp}(\theta_m^r - \theta_m) + K_iG\left(\dot{\theta}_m^r - \dot{\theta}_m\right) + \hat{J}_m\ddot{\theta}_m^r + \hat{B}_m\dot{\theta}_m^r - B_m\dot{\theta}_m \\ +\hat{\tau}_m^{sc} - \tau_m^{sc} + \sum\limits_{i=1}^{n}\left(\hat{L}_i\sin(\hat{\omega}_i\theta_m^r + \hat{\varphi}_i)\right) - \sum\limits_{i=1}^{N}\left(L_i\sin(\omega_i\theta_m + \varphi_i)\right) \\ +\delta\tau_m \end{pmatrix} \tag{10}$$

The modeling errors are defined in Equations (11) and (12):

$$\tilde{\tau}_m^{sc} = \hat{\tau}_m^{sc} - \tau_m^{sc} \tag{11}$$

$$\tilde{L}_m = \sum_{i=1}^{n}\left(\hat{L}_i\sin(\hat{\omega}_i\theta_m^r + \hat{\varphi}_i)\right) - \sum_{i=1}^{N}\left(L_i\sin(\omega_i\theta_m + \varphi_i)\right) \tag{12}$$

Equation (10) can be rewritten as Equation (13):

$$J_m\ddot{\theta}_m = \begin{pmatrix} K_iGk_{pp}(\theta_m^r - \theta_m) + K_iG\left(\dot{\theta}_m^r - \dot{\theta}_m\right) + \hat{J}_m\ddot{\theta}_m^r + \hat{B}_m\dot{\theta}_m^r - B_m\dot{\theta}_m \\ +\widetilde{\tau}_m^{sc} + \widetilde{L}_m \\ +\delta\tau_m \end{pmatrix} \tag{13}$$

Equations (14) and (15) represent the equivalent equations:

$$J_m\ddot{\theta}_m = \hat{J}_m\ddot{\theta}_m - \widetilde{J}_m\ddot{\theta}_m \tag{14}$$

$$\hat{B}_m\dot{\theta}_m^r - B_m\dot{\theta}_m = \hat{B}_m\left(\dot{\theta}_m^r - \dot{\theta}_m\right) + \widetilde{B}_m\dot{\theta}_m \tag{15}$$

where $\widetilde{J}_m = \hat{J}_m - J_m$ and $\widetilde{B}_m = \hat{B}_m - B_m$ denote the estimation errors of the equivalent moment of inertia and equivalent viscous friction coefficient, respectively, which also account for the model parameter uncertainty. Thus, Equation (13) can be rewritten as Equations (16)–(18):

$$\hat{J}_m\ddot{\theta}_m - \widetilde{J}_m\ddot{\theta}_m = \begin{pmatrix} K_iGk_{pp}(\theta_m^r - \theta_m) + K_iG\left(\dot{\theta}_m^r - \dot{\theta}_m\right) + \hat{J}_m\ddot{\theta}_m^r + \hat{B}_m\left(\dot{\theta}_m^r - \dot{\theta}_m\right) + \widetilde{B}_m\dot{\theta}_m \\ +\widetilde{\tau}_m^{sc} + \widetilde{L}_m \\ +\delta\tau_m \end{pmatrix} \tag{16}$$

$$0 = \begin{pmatrix} K_iGk_{pp}(\theta_m^r - \theta_m) + \left(K_iG + \hat{B}_m\right)\left(\dot{\theta}_m^r - \dot{\theta}_m\right) + \hat{J}_m\left(\ddot{\theta}_m^r - \ddot{\theta}_m\right) \\ +\widetilde{J}_m\ddot{\theta}_m + \widetilde{B}_m\dot{\theta}_m + \widetilde{\tau}_m^{sc} + \widetilde{L}_m \\ +\delta\tau_m \end{pmatrix} \tag{17}$$

$$\hat{J}_m\ddot{\widetilde{\theta}}_m + \left(K_iG + \hat{B}_m\right)\dot{\widetilde{\theta}}_m + K_iGk_{pp}\widetilde{\theta}_m = \eta + \delta\tau_m \tag{18}$$

where $\ddot{\widetilde{\theta}}_m = \left(\ddot{\theta}_m - \ddot{\theta}_m^r\right)$, $\dot{\widetilde{\theta}}_m = \left(\dot{\theta}_m - \dot{\theta}_m^r\right)$, $\widetilde{\theta}_m = (\theta_m - \theta_m^r)$, and $\eta = \widetilde{J}_m\ddot{\theta}_m + \widetilde{B}_m\dot{\theta}_m + \widetilde{\tau}_m^{sc} + \widetilde{L}_m$. Here, η simultaneously represents the model parameter uncertainty and modeling errors. If the Euclidean norm $\|\eta\|$ of η is less than that of ρ (i.e., $\|\eta\| < \rho$), $\delta\tau_m$ can be designed to mitigate the influence of η.

Equations (19)–(21) are defined as follows:

$$G = k_{vp}\left(1 + \frac{1}{T_i s}\right) \tag{19}$$

$$\left(K_iG + \hat{B}_m\right) = \left(K_ik_{vp} + \hat{B}_m\right) + \left(\frac{K_ik_{vp}}{T_i s}\right) = \alpha_0 + \alpha_1\frac{1}{s} \tag{20}$$

$$K_iGk_{pp} = K_ik_{vp}k_{pp} + \frac{K_ik_{vp}k_{pp}}{T_i s} = \beta_0 + \beta_1\frac{1}{s} \tag{21}$$

where $\alpha_0 = K_ik_{vp} + \hat{B}_m$, $\alpha_1 = \frac{K_ik_{vp}}{T_i}$, $\beta_0 = K_ik_{vp}k_{pp}$, and $\beta_1 = \frac{K_ik_{vp}k_{pp}}{T_i}$. Equation (18) can be rewritten as Equation (22):

$$\hat{J}_m\ddot{\widetilde{\theta}}_m + \alpha_0\dot{\widetilde{\theta}}_m + \alpha_1\int\dot{\widetilde{\theta}}_m dt + \beta_0\widetilde{\theta}_m + \beta_1\int\widetilde{\theta}_m dt = \eta + \delta\tau_m \tag{22}$$

Moreover, the state variables are defined in Equations (23)–(25):

$$x_1 = \int\widetilde{\theta}_m dt \tag{23}$$

$$x_2 = \widetilde{\theta}_m \tag{24}$$

$$x_3 = \dot{\widetilde{\theta}}_m \tag{25}$$

Under zero initial conditions, Equation (22) can be rewritten as a state equation, as shown in Equation (26):

$$\begin{bmatrix} \dot{x}_1 \\ \dot{x}_2 \\ \dot{x}_3 \end{bmatrix} = \begin{bmatrix} 0 & 1 & 0 \\ 0 & 0 & 1 \\ -\frac{\beta_1}{\hat{J}_m} & -\frac{\alpha_1+\beta_0}{\hat{J}_m} & -\frac{\alpha_0}{\hat{J}_m} \end{bmatrix} \begin{bmatrix} x_1 \\ x_2 \\ x_3 \end{bmatrix} + \begin{bmatrix} 0 \\ 0 \\ \frac{1}{\hat{J}_m} \end{bmatrix} (\eta + \delta\tau_m) \tag{26}$$

The error vector e is defined in Equation (27), and the matrix A and vector b are defined by Equations (28) and (29), respectively:

$$e = \begin{bmatrix} x_1 & x_2 & x_3 \end{bmatrix}^T \tag{27}$$

$$A = \begin{bmatrix} 0 & 1 & 0 \\ 0 & 0 & 1 \\ -\frac{\beta_1}{\hat{J}_m} & -\frac{\alpha_1+\beta_0}{\hat{J}_m} & -\frac{\alpha_0}{\hat{J}_m} \end{bmatrix} \tag{28}$$

$$b = \begin{bmatrix} 0 & 0 & \frac{1}{\hat{J}_m} \end{bmatrix}^T \tag{29}$$

Therefore, Equation (26) can be rewritten as the error equation in Equation (30):

$$\dot{e} = Ae + b(\eta + \delta\tau_m) \tag{30}$$

Because $\|\eta\| < \rho$, according to Theorem 1, this study designed an additional compensation term $\delta\tau_m$ as Equation (31), such that the solution trajectory of the error equation presented as Equation (30) is bounded.

$$\delta\tau_m = \begin{cases} -\rho\frac{b^T Pe}{\|b^T Pe\|}, \|b^T Pe\| > \sigma \\ -\frac{\rho}{\sigma} b^T Pe, \|b^T Pe\| \leq \sigma \end{cases} \tag{31}$$

where σ is a threshold constant, and $\|b^T Pe\|$ denotes the Euclidean norm of $(b^T Pe)$. Matrix A must be stable, and matrices $P = P^T > 0$ and $Q = Q^T > 0$ must satisfy the Lyapunov equation presented in Equation (32):

$$A^T P + PA = -Q \tag{32}$$

Theorem 1. *The additional compensation term $\delta\tau_m$ presented in Equation (31) ensures that the solution trajectory of the error equation in Equation (30) remains bounded.*

Proof. Considering the error equation in Equation (30), the Lyapunov function is defined in Equation (33):

$$V = e^T Pe \tag{33}$$

where matrix $P = P^T > 0$. By differentiating Equation (33), the derivative of the Lyapunov function can be obtained using Equation (34):

$$\dot{V} = \dot{e}^T Pe + e^T P\dot{e} \tag{34}$$

Substituting Equation (30) into Equation (34), Equation (34) can be substituted into Equation (35):

$$\dot{V} = \left(e^T A^T Pe + e^T PAe\right) + 2\left(e^T Pb\right)(\eta + \delta\tau_m) \tag{35}$$

Subsequently, referring to Equation (32), Equation (35) can be rewritten as Equation (36):

$$\dot{V} = -e^T Qe + 2\left(b^T Pe\right)^T (\eta + \delta\tau_m) \tag{36}$$

Because $\|\eta\| < \rho$, Equation (37) can be derived from Equation (36):

$$\dot{V} < -e^T Qe + 2\left(b^T Pe\right)^T \left(\rho \frac{b^T Pe}{\|b^T Pe\|} + \delta\tau_m\right) \tag{37}$$

If the additional compensation term $\delta\tau_m$ is designed using Equation (31) and $\|b^T Pe\| > \sigma$, then $\delta\tau_m = -\rho\frac{b^T Pe}{\|b^T Pe\|}$ and $\dot{V} < 0$ because $2\left(b^T Pe\right)^T \left(\rho\frac{b^T Pe}{\|b^T Pe\|} + \delta\tau_m\right) = 0$ and $Q = Q^T > 0$. However, when the additional compensation term $\delta\tau_m$ is designed using Equation (31) and $\|b^T Pe\| \leq \sigma$, then $\delta\tau_m = -\frac{\rho}{\sigma}b^T Pe$ and $2\left(b^T Pe\right)^T \left(\rho\frac{b^T Pe}{\|b^T Pe\|} + \delta\tau_m\right) = 2\rho\|b^T Pe\| - 2\frac{\rho}{\sigma}\|b^T Pe\|^2$. Here, Equation (37) can be rewritten as Equation (38):

$$\dot{V} < -e^T Qe + 2\rho\left\|b^T Pe\right\| - 2\frac{\rho}{\sigma}\left\|b^T Pe\right\|^2 \tag{38}$$

As the minimum eigenvalue of the matrix Q, $\lambda_{\min}(Q)$, satisfies the inequality $\lambda_{\min}(Q)\|e\|^2 \leq e^T Qe$, to achieve $\dot{V} < 0$, Equation (39) must be satisfied:

$$2\frac{\rho}{\sigma}\left\|b^T Pe\right\|^2 - 2\rho\left\|b^T Pe\right\| + \lambda_{\min}(Q)\|e\|^2 > 0 \tag{39}$$

where $\|e\|$ denotes the Euclidean norm of the error vector e. Furthermore, because Equation (39) is a quadratic inequality of $\left\|b^T Pe\right\|$ and the minimal value is $-\frac{\rho\sigma}{2} + \lambda_{\min}(Q)\|e\|^2$ when $\left\|b^T Pe\right\| = \frac{\sigma}{2}$, the matrix Q must satisfy the inequality presented in Equation (40) to achieve $\dot{V} < 0$:

$$-\frac{\rho\sigma}{2} + \lambda_{\min}(Q)\|e\|^2 > 0 \tag{40}$$

In other words, when $\left\|b^T Pe\right\| \leq \sigma$ and matrix Q satisfy Equation (40), $\dot{V} < 0$ and $\|e\| > \sqrt{\frac{\rho\sigma}{2\lambda_{\min}(Q)}}$.

Accordingly, when $\left\|b^T Pe\right\| > \sigma$, a set S_A exists, such that the solution trajectory of Equation (30) will reach and remain within set S_A. Moreover, when $\left\|b^T Pe\right\| \leq \sigma$, a set S_B exists, and the properties of $\|e\| \leq \sqrt{\frac{\rho\sigma}{2\lambda_{\min}(Q)}}$ and $S_B \subseteq S_A$ hold. Therefore, the additional compensation term $\delta\tau_m$ is designed in Equation (31) to ensure that the solution trajectory of Equation (30) is limited between the sets S_A and S_B, suggesting that the solution trajectory of Equation (30) is bounded. □

Equations (8), (31), and (32) construct RDC. As shown in Figure 4, the additional compensation term $\delta\tau_m$ is calculated using Equations (31) and (32) with the angular position command θ_m^r, angular velocity command $\dot{\theta}_m^r$, and angular acceleration command $\ddot{\theta}_m^r$ of the PMSM along with its actual angular position θ_m and actual angular velocity $\dot{\theta}_m$. Subsequently, the driving torque τ_m of the PMSM is calculated using Equation (8). For simplicity, this study designed the matrix $Q = q \cdot I$, where q is a positive and real variable. Therefore, the RDC provides the control parameters k_{pp}, k_{vp}, T_i, ρ, σ, and q. The conservative design of control parameters generally increases the stability of the control system but may limit the running performance of the RDC. Conversely, improving running performance often results in reduced stability. Therefore, considering the complexity of the control parameter design, this study utilized a manual approach to adjust the control parameters based on their properties. According to Equations (28) and (30), the control parameters k_{pp}, k_{vp}, and T_i determine the dynamic response of the solution trajectory of the error equation presented in Equation (30). This study adopted the common control-parameter-adjustment rule mentioned previously to adjust the control parameters k_{pp}, k_{vp}, and T_i. Referring to Equation (31), the threshold constant σ influences the chattering phenomenon of the

solution trajectory. To suppress the chattering, this study adjusted the threshold constant σ. A larger boundary constant ρ enhances the stability of the control system; however, a larger boundary constant ρ frequently increases the response time and steady-state error of the control system. According to Theorem 1, the Euclidean norm of the solution trajectory is proportional to the product of the boundary constant ρ and the threshold constant σ and inversely proportional to the control parameter q. Therefore, this study adjusted the control parameters ρ, σ, and 24 to decrease the product of the boundary constant ρ and threshold constant σ while increasing the control parameter q to achieve stable motions of the PMSM-driven rotary machine with reduced position errors.

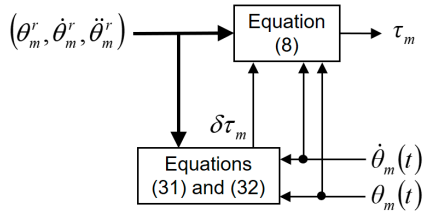

Figure 4. RDC design based on the P-PI feedback-and-compensation control structure.

4. Experiment

This study employed a PMSM test bench, as depicted in Figure 5, consisting primarily of load and drive motors. The drive motor was connected to the load motor through two couplers and a connection rod to facilitate various control experiments. Both drive and load motors were PMSMs. The drive motor had a rated power of 2.0 kW, rated speed of 2000 rpm, rated torque of 9.55 Nm, and torque constant of 0.868 Nm/A. The drive motor was equipped with a 22-bit absolute encoder to detect the actual angular position of the drive motor. The FPGA-based cRIO control console developed by National Instruments (NI) was used on the EtherCAT fieldbus industrial network system to manage the drive motor through a PMSM driver. The NI LabVIEW 2016 software integrated the control system, including the human–machine operating interface, signal measurement and control, and recording and displaying of experimental data. The PMSM driver used to actuate the drive motor comprised the control and power stages. The physical control of the drive motor was implemented on the power stage, and current control was implemented on the control stage of the PMSM driver. The driving torque calculated by different control methods was converted to the driving current command sent to the current control in the control stage to actuate the PMSM. Through the EtherCAT network, the cRIO control console transmitted the control command (current command) to the PMSM driver and received feedback signals (position and velocity signals) within a sampling period of 1.0 ms. The cRIO control console generated motion commands such as the position, velocity, and acceleration commands for identifying position-dependent periodic disturbances and parameters of the PMSM test bench and for performing motion control experiments. Figure 5 shows the program flow implemented on the cRIO control console for motion control experiments with different control methods.

This study utilized constant-speed and moment-of-inertia estimation experiments [32] to identify the parameters of the test bench, as shown in Table 1. The characteristics of position-dependent periodic disturbance were analyzed through offline experiments [32]. Figure 6 shows the estimated position-dependent periodic disturbance on the drive motor side of the test bench after removing the average. To demonstrate the periodic disturbance property of the position-dependent periodic disturbance, Figure 6 presents the position-dependent periodic disturbance estimation results for a complete turn. The position-dependent periodic disturbances exhibited periodic fluctuations. Spatial FFT was used to analyze the spatial spectrum of the disturbance torque, revealing the distribution of the position-dependent periodic disturbance.

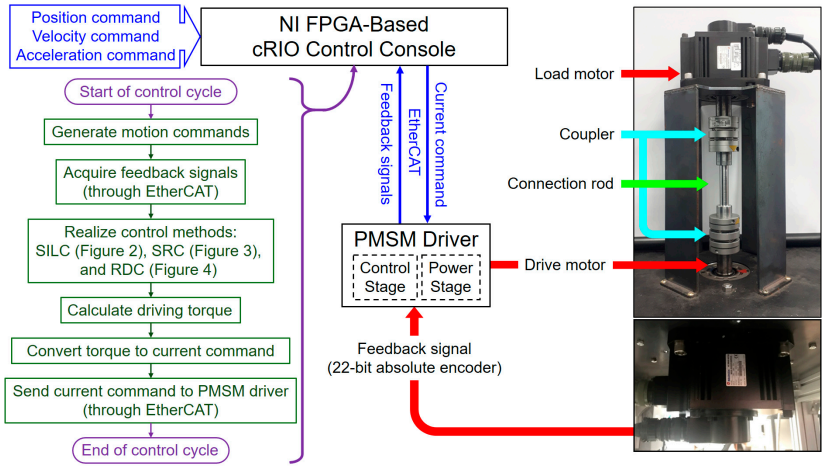

Figure 5. The PMSM test bench used in this study.

Table 1. Parameters of the PMSM test bench.

Parameter	Value
Equivalent moment of inertia	0.780×10^{-2} kg-m^2
Equivalent viscous friction coefficient	0.339×10^{-1} Nm/rad/s
Coulomb friction torque	0.387 Nm
Static friction torque	0.457 Nm
Stribeck velocity	0.551 rad/s
Stribeck shape factor	1.957

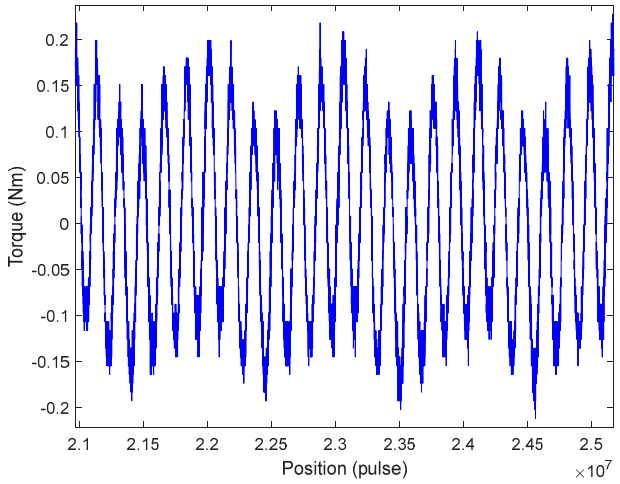

Figure 6. Position-dependent periodic disturbance estimation results (for a complete turn).

Figure 7 shows the spatial FFT results corresponding to the position-dependent periodic disturbance, as shown in Figure 6. Figure 7 illustrates the periodic properties of the disturbance torque and highlights the relative importance of the spatial-frequency components of the periodic disturbance. This revealed that the periodic disturbance had two main components: 5.724×10^{-6} (encoder increment, EI)$^{-1}$ (magnitude of 0.140) and 9.678×10^{-7} (EI)$^{-1}$ (magnitude of 0.022). The first main component 5.724×10^{-6} (EI)$^{-1}$ indicated that the disturbance torque period approximated 174713 EI, suggesting that the periodic disturbance torque completes one cycle in approximately every 174713 encoder pulses. The second main component, the 9.678×10^{-7} (EI)$^{-1}$, indicated that the periodic disturbance torque completed one cycle for approximately every 1033304 encoder pulses. Because the drive motor uses a 22-bit absolute encoder, the main components 5.724×10^{-6} (EI)$^{-1}$ and 9.678×10^{-7} (EI)$^{-1}$

also implied that within each revolution of the drive motor, 24 and 4 fluctuations appeared in the position-dependent periodic disturbance, respectively, as shown in Figure 6.

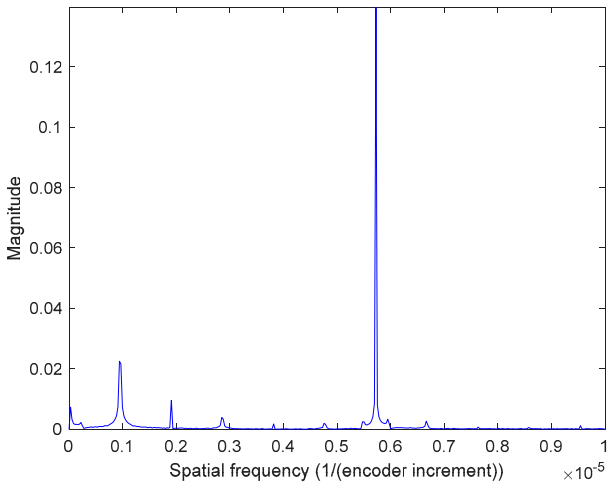

Figure 7. Spatial FFT of the position-dependent periodic disturbance (corresponding to Figure 6).

By analyzing the spatial FFT of the position-dependent periodic disturbance, the parameters for the drive motor side of the test bench, as shown in Figure 6, included the spatial frequency 5.724×10^{-6} $(\mathrm{EI})^{-1}$ with a magnitude of 0.140 Nm and phase of 1.275 rad and the spatial frequency 9.678×10^{-7} $(\mathrm{EI})^{-1}$ with a magnitude 0.022 Nm and phase of 0.521 rad. Figure 8 shows the modeled disturbance torque. The position-dependent periodic disturbance model developed in this study effectively captured and presented the spatial frequency, magnitude, and phase features of the disturbance torque.

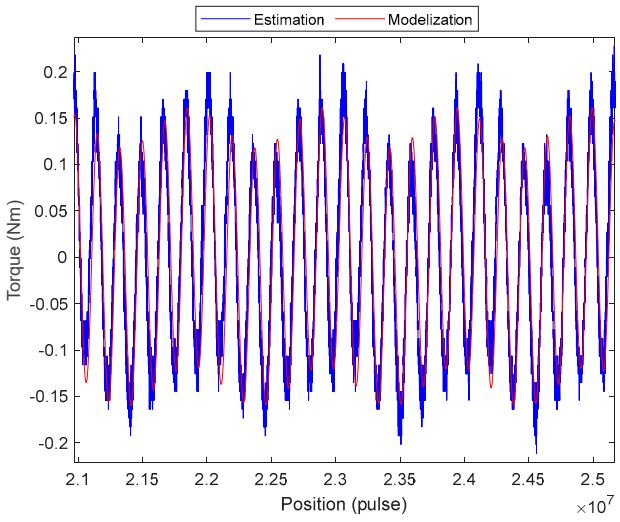

Figure 8. Position-dependent periodic disturbance estimation and modeling.

In the experiments, a ramp position command was applied to the drive motor of the test bench, expressed in Equation (41), where θ_m^r represents the angular position command of the drive motor (in radians), and n_m^r denotes the velocity command (in rpm). Equation (41) also indicates that the drive motor completed ten full turns in each experiment, with one turn corresponding to 4, 194, 304 pulses owing to the 22-bit encoder equipped on the drive motor.

$$\theta_m^r(t) = \begin{cases} n_m^r\left(\frac{2\pi}{60}\right) \cdot t, \text{ if } \theta_m^r(t) < 20\pi \\ 20\pi, \text{ if } \theta_m^r(t) \geq 20\pi \end{cases} \tag{41}$$

To validate the feasibility and running performance of the RDC, this study conducted experiments using velocity commands of 10, 15, and 20 rpm. The control structures compared include SILC (Section 2.3), SRC (Section 2.4), and RDC (Section 3). In addition, this study utilized the average value (AVG) of the position error (i.e., angular position command minus actual angular position), root-mean-square value (RMS), and maximum absolute value (MAX) as performance indices to analyze the experimental results.

4.1. Experimental Results of SILC

Figure 9 shows the experimental results of operating the drive motor with SILC over ten turns. To emphasize the suppression effect of the control structure on the position-dependent periodic disturbance, the vertical axis represents the RMS after removing the AVG of the position error for each turn, whereas the horizontal axis denotes the turn number. The experimental results revealed that during the first turn, a larger error occurred owing to the transient-state response and that the error increased as the velocity command increased. However, as the SILC learning process progressed, the error decreased from the second turn onwards and converged by the fifth turn. For a velocity command of 10 rpm, the error decreased from 3.723×10^{-3} rad (first turn) to 0.327×10^{-3} rad (tenth turn) with a reduction rate of 91.21%. When the velocity command was increased to 15 and 20 rpm, the error reduction rates were 94.48% and 96.52%, respectively. Figure 9 illustrates the effectiveness of the SILC in suppressing the disturbance torque at different velocity commands. At 10 rpm, the error reduction rate from the first to the second turn is 43.16%; however, when the velocity command increased to 15 and 20 rpm, the error reduction rates for the second and first turns increased to 68.79% and 78.63%, respectively. These results demonstrate that SILC effectively mitigates the adverse effects of position-dependent periodic disturbances on the positional motion of a drive motor.

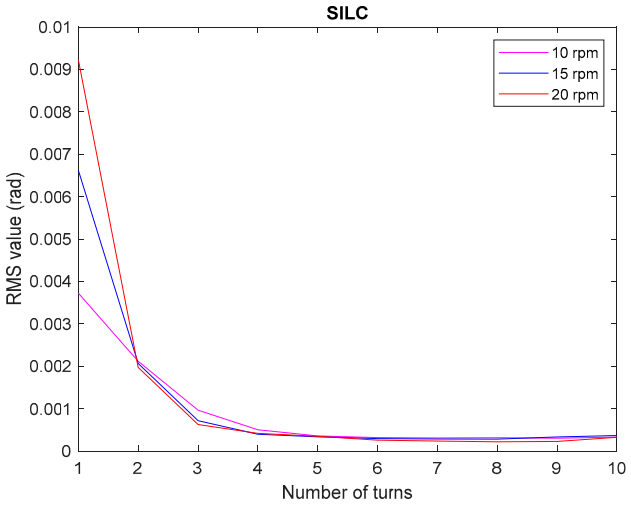

Figure 9. Experimental results of the drive motor operating for ten turns (SILC).

Figure 10 shows the experimental results of the drive motor during the first, second, and tenth turns using the SILC with different velocity commands. It also shows the transient-state (first and second turns) and steady-state (tenth turn) operating conditions of the drive motor. To highlight the impact of position-dependent periodic disturbances on the positional motions of the drive motor, the position error (after subtracting the AVG of each turn) is depicted in a polar coordinate frame. The results indicated that the drive motor with different velocity commands exhibited significant transient-state errors during the first turn, with error magnitudes ranging from 15° (occurring at a velocity command of 10 rpm) to 45° (occurring at a velocity command of 20 rpm). Specifically, the MAX values of the transient-state errors for velocity commands of 10, 15, and 20 rpm were 3.007×10^{-2} rad, 5.222×10^{-2} rad, and 6.564×10^{-2} rad, respectively. As the drive motor progressed to the

second turn, the SILC started to mitigate the error, resulting in a decrease. The tenth turn significantly reduced the error compared with the first and second turns. For the tenth turn, the MAX values of the steady-state errors for velocity commands of 10, 15, and 20 rpm were 1.011×10^{-3} rad, 1.278×10^{-3} rad, and 1.912×10^{-3} rad, respectively. Although SILC effectively suppressed position-dependent periodic disturbances, the learning process before convergence still exhibited larger error values. The ILC law affects the learning period of SILC, thereby influencing the convergence time of the position error during PMSM operation.

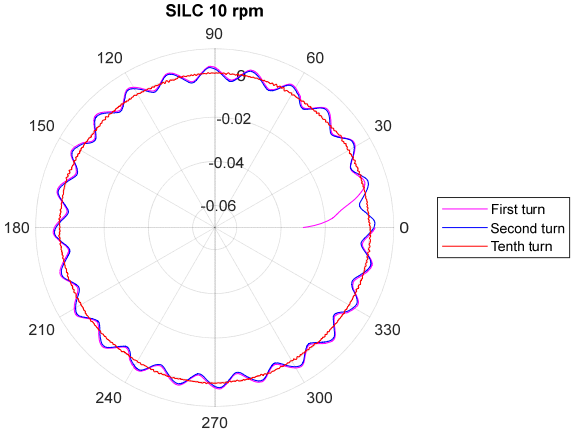

(**a**) 10 rpm

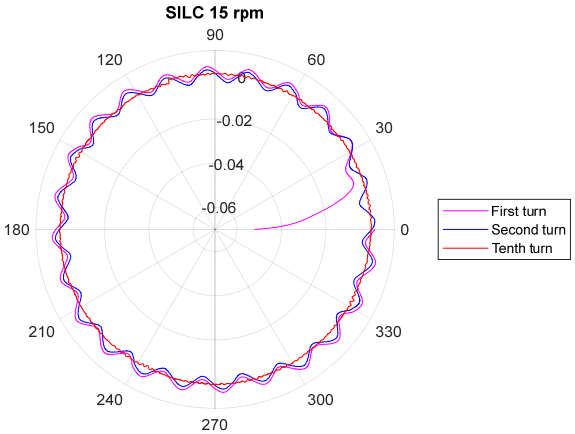

(**b**) 15 rpm

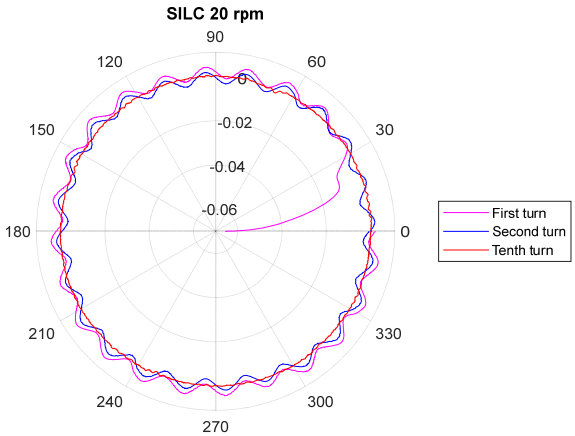

(**c**) 20 rpm

Figure 10. Experimental results of transient-state and steady-state operation of the drive motor (SILC) (circular angle axis unit: degree; radial axis unit: radian).

4.2. Experimental Results of SRC

Figure 11 presents the experimental results of the drive motor using SRC over ten turns under various velocity commands. As observed, owing to the influence of the transient-state response, the drive motor exhibited a larger position error in the first turn across all velocity commands. However, SRC ensured that the position error began to converge by the second turn. For the velocity commands of 10, 15, and 20 rpm, the error reduction rates for the second and first turns were 91.67%, 89.86%, and 88.58%, respectively. The corresponding error reduction rates from the tenth and first turns were 91.29%, 91.30%, and 92.18%, respectively. Compared with the SILC experimental results shown in Figure 9, SRC effectively mitigates the adverse effects of position-dependent periodic disturbances and facilitates a more rapid convergence of the position error during a drive motor operation.

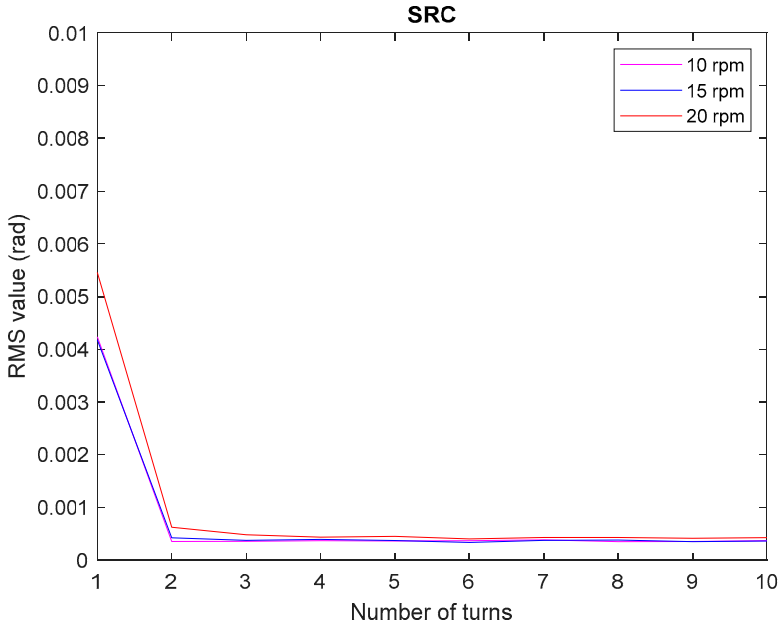

Figure 11. Experimental results of drive motor operating for ten turns (SRC).

Figure 12 shows the experimental results for the drive motor during the first, second, and tenth turns. The drive motor also exhibited a significant transient-state error during the first turn, with the error range expanding as the velocity command increased. For a velocity command of 10 rpm, the range of influence of the transient-state error was approximately 180°. However, when the velocity command was increased to 20 rpm, the influence range of the transient-state error increased to approximately 360°. By comparison, SILC began to converge on the position error by the fifth turn. Although the range of the influence of the transient-state error of SRC was larger, SRC caused the position error of the drive motor to converge by the second turn. Moreover, the MAX values of the transient-state errors for velocity commands of 10, 15, and 20 rpm were 1.888×10^{-2} rad, 1.793×10^{-2} rad, and 2.884×10^{-2} rad, respectively, which were significantly lower than those observed with SILC. By the second turn, SRC began to effectively reduce the position error. By the tenth turn, the MAX values of the velocity commands of 10, 15, and 20 rpm were 0.907×10^{-3} rad, 0.902×10^{-3} rad, and 0.988×10^{-3} rad, respectively. These results indicated that, similar to SILC, SRC can effectively suppress the adverse effects of position-dependent periodic disturbances on the positional motions of a drive motor. Moreover, SRC achieves a faster convergence of the position error, thereby significantly addressing the learning period problems associated with SILC.

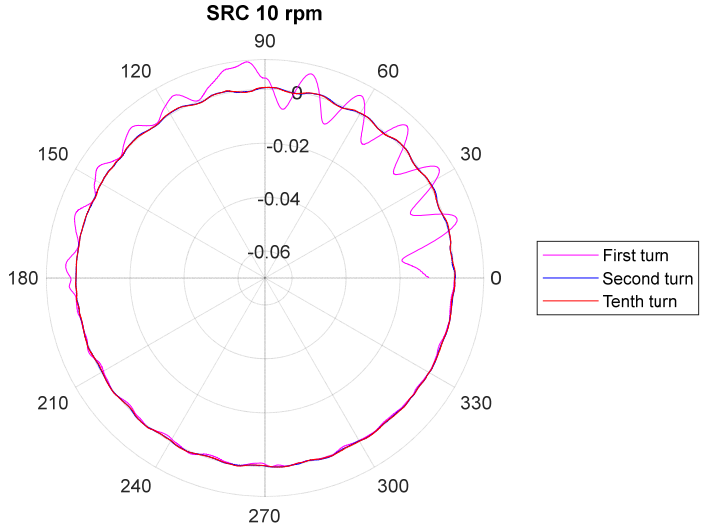

(**a**) 10 rpm

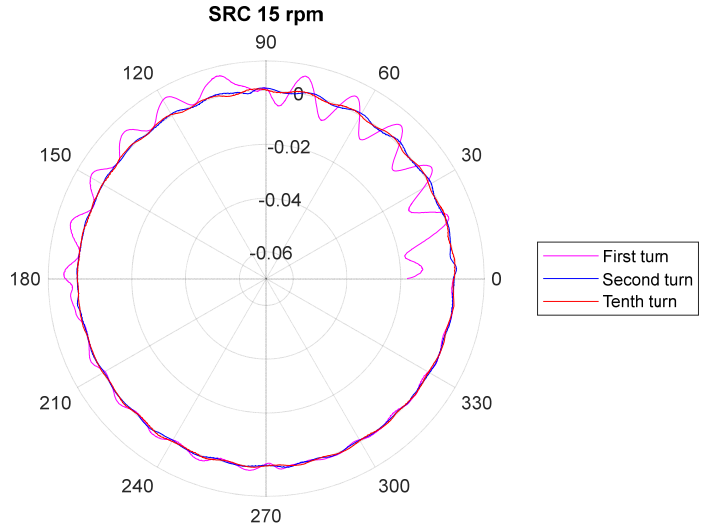

(**b**) 15 rpm

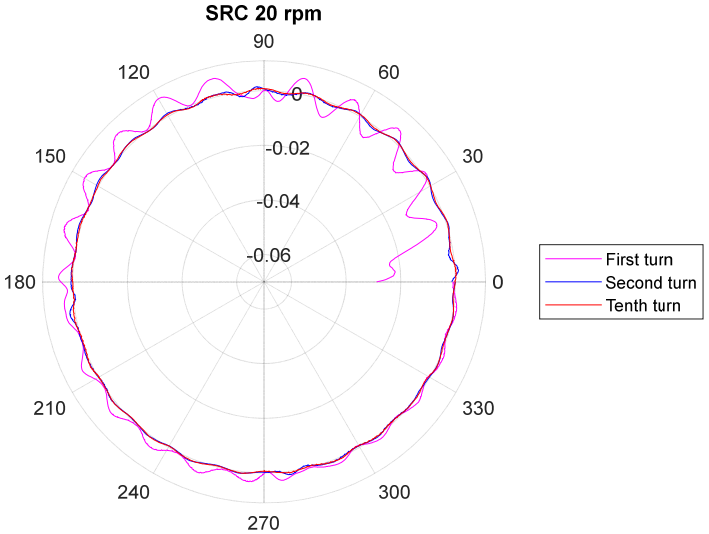

(**c**) 20 rpm

Figure 12. Experimental results of transient-state and steady-state operation of the drive motor (SRC) (circular angle axis unit: degree; radial axis unit: radian).

4.3. Experimental Results of RDC

Figure 13 presents the experimental results of the drive motor using RDC over ten turns of operation under varying velocity commands. Although a larger position error was observed during the first turn owing to the transient-state response, RDC significantly reduced this error compared with SILC and SRC, with the maximum error being merely 1.888×10^{-3} rad. Regarding the error convergence, RDC did not exhibit a learning process, which means that the error began to converge by the second turn. By the tenth turn, the error with RDC approached the levels observed with SRC and SILC, with the maximum error being 0.515×10^{-3} rad. Thus, by comparing Figure 9, Figure 11, and Figure 13, it is evident that RDC achieved the smallest position error during the first turn of the operation. Additionally, both RDC and SRC resulted in position error convergence by the second turn. Thus, RDC provides a position-dependent periodic disturbance suppression effect comparable to that of SRC and SILC.

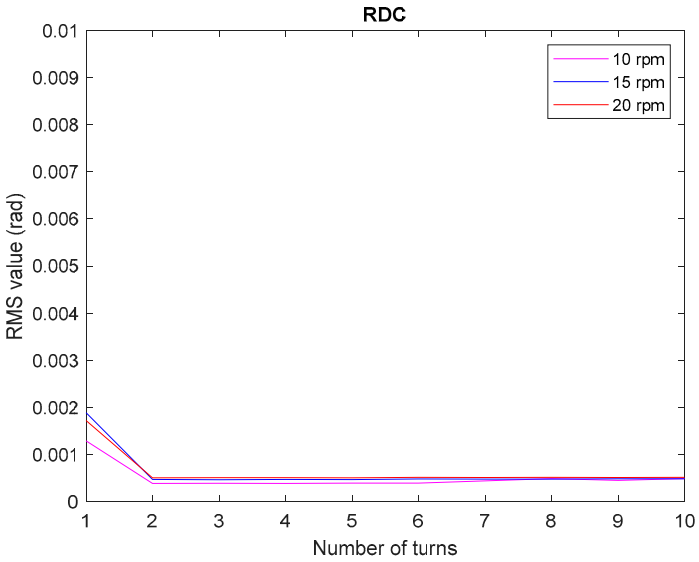

Figure 13. Experimental results of the drive motor operating for ten turns (RDC).

Figure 14 shows the transient-state and steady-state operating results of the drive motor for different velocity commands. Although a transient-state error was evident during the first turn, its range was limited from 15° to 30°, which was lower than the influence ranges observed for both SILC and SRC. Thus, while both RDC and SRC achieved position error convergence by the second turn (see Figures 11 and 13), the RDC exhibited a more rapid position error convergence rate. Additionally, the MAX values for velocity commands of 10, 15, and 20 rpm were 1.275×10^{-2} rad, 1.426×10^{-2} rad, and 1.451×10^{-2} rad, respectively. These values were lower than those of SRC and significantly lower than those of SILC.

Because of its faster error convergence, RDC enabled the drive motor to reach a steady state by the first turn and maintain it through the tenth turn. For velocity commands of 10, 15, and 20 rpm, the MAX values of the position error reduction rates of the tenth and first turns were 85.67%, 90.78%, and 90.65%, respectively. The experimental results indicated that, similar to SRC and SILC, RDC effectively mitigates the adverse effects of position-dependent periodic disturbances and achieves a steady-state position comparable to that of SRC and SILC. Moreover, RDC offers a higher convergence rate and smaller transient-state error than SRC and SILC. Similar to SRC, RDC does not exhibit the learning period problem inherent to SILC.

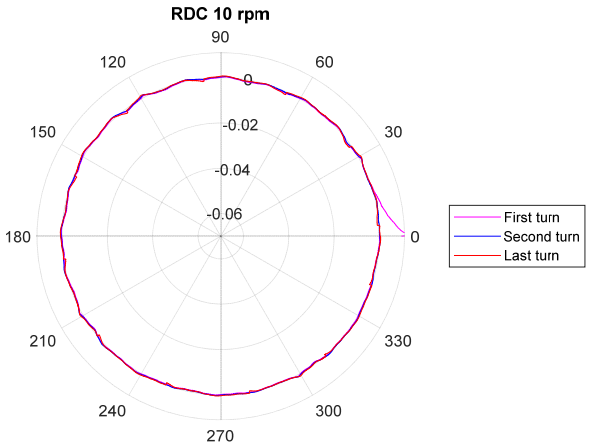

(**a**) 10 rpm

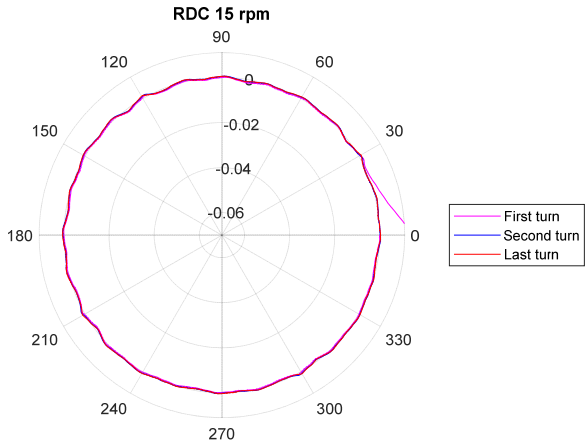

(**b**) 15 rpm

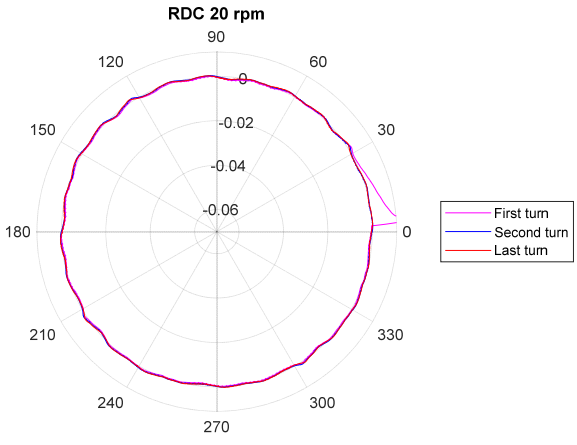

(**c**) 20 rpm

Figure 14. Experimental results of transient-state and steady-state operation of the drive motor (RDC) (circular angle axis unit: degree; radial axis unit: radian).

4.4. Position Error Analysis

Figures 9–14 present the position error of each turn after removing the AVG of the position error of the turn. These figures facilitate the analysis of the influence and suppression effects of different control structures on position-dependent periodic disturbances. However, because the control structure also affects the dynamic characteristics of the drive motor during operation, a comprehensive analysis of the position error is necessary to fully understand the effects of and improvements in the control structure on the positional motion performance of the drive motor.

Figures 15 and 16 show the position errors of the drive motor during the first three turns and the tenth turn of the operation with various velocity commands. The position error for the first three turns denotes a transient-state operation, whereas that for the tenth turn represents a steady-state operation. Both SILC and SRC exhibited significant transient-state and steady-state errors. Additionally, owing to the learning process associated with SILC, the convergence to a steady-state error was slower than that of SRC.

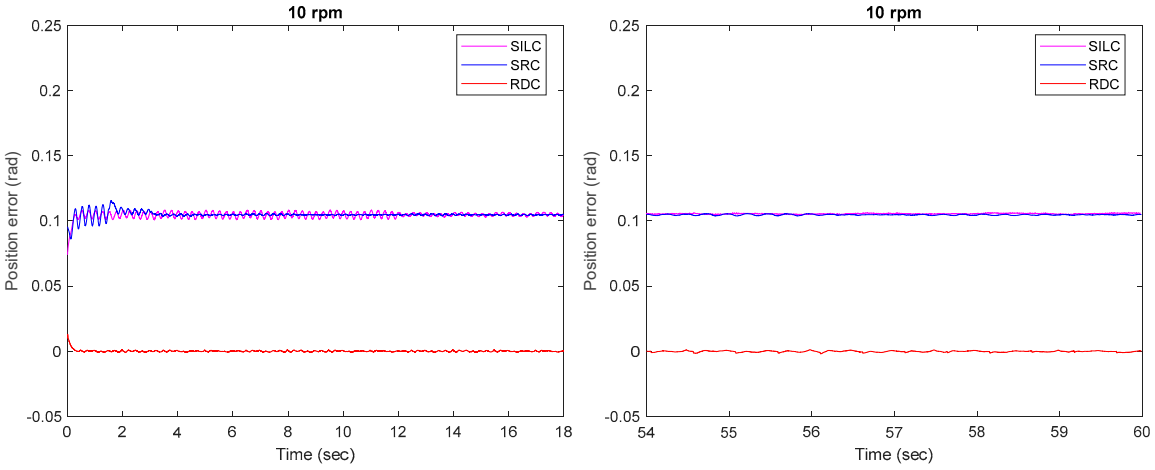

(**a**) 10 rpm

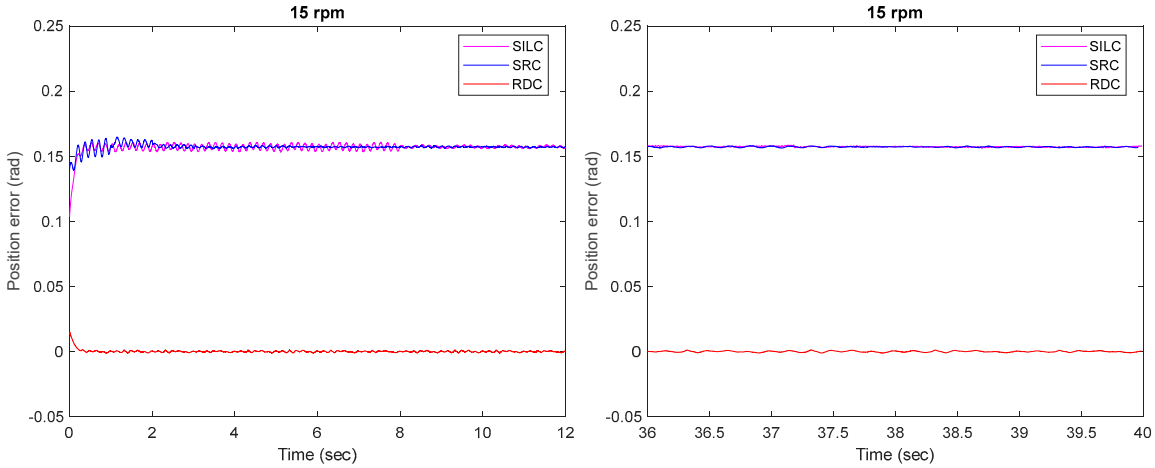

(**b**) 15 rpm

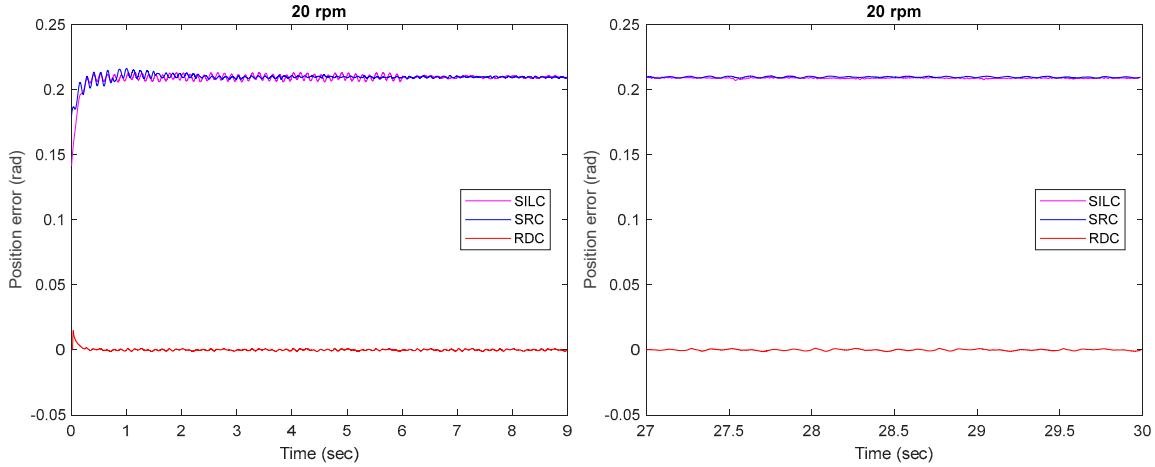

(**c**) 20 rpm

Figure 15. Position error in the drive motor operating process (left: first three turns; right: tenth turn).

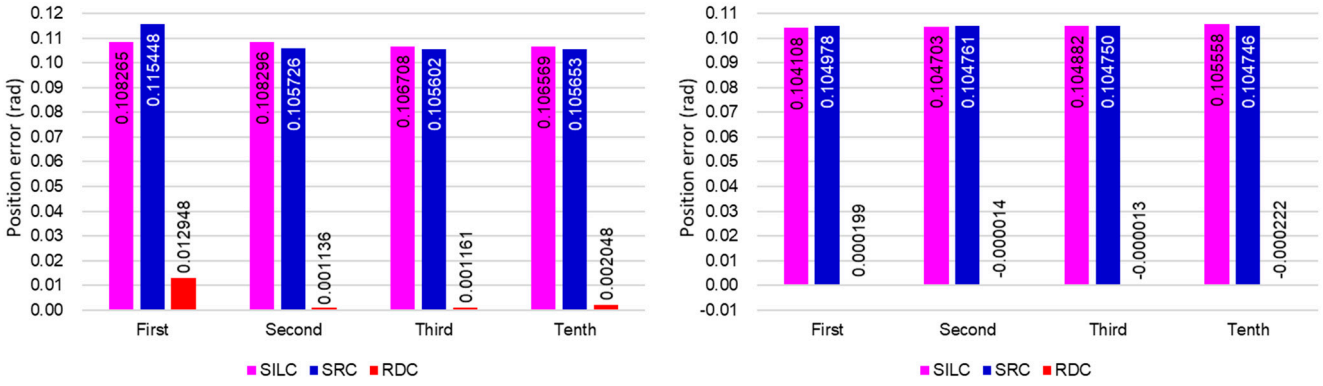

(**a**) 10 rpm

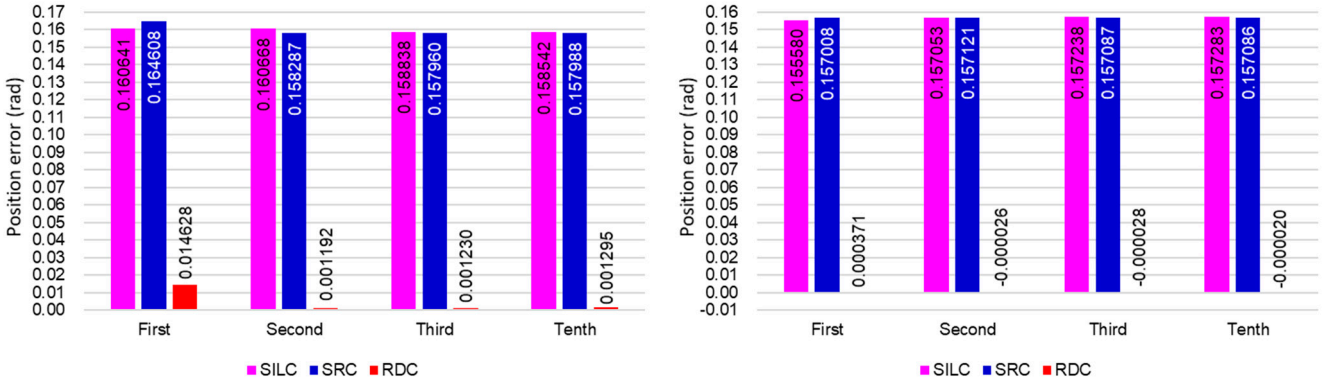

(**b**) 15 rpm

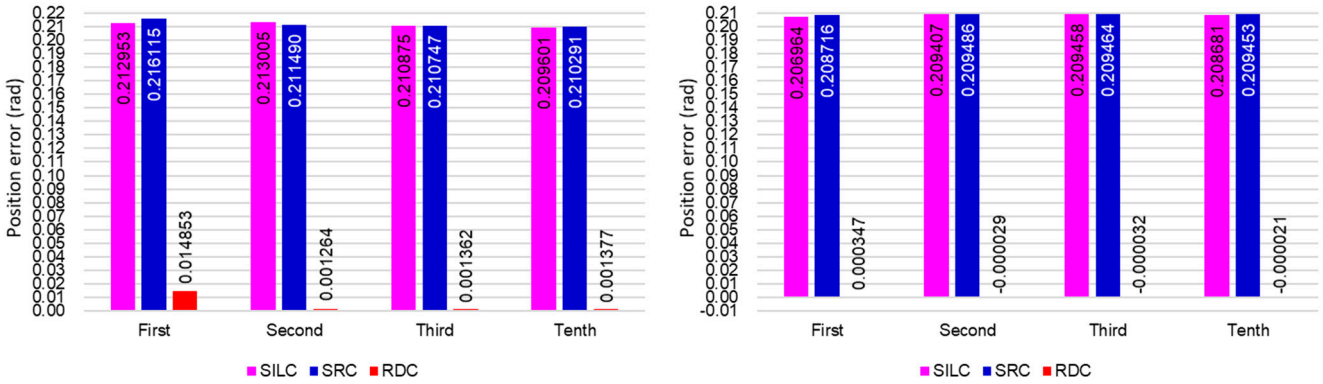

(**c**) 20 rpm

Figure 16. Comparison of MAX and AVG position errors (left: MAX; right: AVG).

When the drive motor operated under a velocity command of 10 rpm, the MAX of the transient-state error of SILC was 0.108 rad, and that of the transient-state error of SRC was 0.115 rad. As the velocity command increased to 20 rpm, the MAX values of the transient-state errors of SILC and SRC increased to 0.213 rad and 0.216 rad, respectively. In contrast, RDC achieved a lower error when operating with different velocity commands. When the velocity commands were 10, 15, and 20 rpm, the MAX of the transient-state error of the RDC were 1.295×10^{-2} rad, 1.463×10^{-2} rad, and 1.485×10^{-2} rad, respectively.

For the tenth turn of operation under a velocity command of 10 rpm, the AVG of the steady-state errors for SILC and SRC were 0.106 rad and 0.105 rad, respectively. Moreover, when the velocity commands increased to 20 rpm, the AVG of the steady-state errors of SILC and SRC also increased to 0.209 rad and 0.209 rad, respectively. The experimental results

indicated that while both SILC and SRC effectively suppressed position-dependent periodic disturbances, the dynamic characteristics of the drive motor made the AVG of the steady-state error of SILC and SRC larger and susceptible to velocity commands. Compared with the SILC and SRC, the RDC achieved smaller steady-state errors across different velocity commands. As the velocity command changed, the AVG of the steady-state error of the RDC became lower than 0.001 rad, whereas the error reduction rates all reached 90%. Accordingly, RDC not only provides a position-dependent periodic disturbance suppression effect similar to SRC and SILC but also smaller transient-state and steady-state position errors.

5. Conclusions

The accuracy and smoothness of positional motion in PMSM-driven rotary machines are crucial for industrial applications. However, position-dependent periodic disturbances, which exhibit periodic variations based on the rotational angle, often affect and limit the motion performance of PMSM-driven rotary machines.

The period of the position-dependent periodic disturbances varies with the motion velocity of a PMSM-driven rotary machine, often rendering traditional disturbance estimation and compensation methods, including temporal ILC and temporal RC, ineffective in suppressing these disturbances. While SILC and SRC can suppress position-dependent periodic disturbances, SILC encounters challenges related to the computational burden and convergence time of the learning process, whereas SRC does not significantly improve the transient-state motion performance owing to the inherent dynamics of the rotary machine. Therefore, the RDC developed in this study can effectively address these problems by significantly suppressing position-dependent periodic disturbances and enhancing the overall motion performance of PMSM-driven rotary machines.

This study referred to the P-PI feedback control structure widely used in commercial PMSM drives, the dynamic characteristics of PMSM-driven rotary machines, and the parameter uncertainties and modeling errors in both the dynamic and disturbance models to develop an RDC with dynamic and disturbance compensation by employing a robust control approach. Additionally, this study created a position-dependent periodic disturbance model using multiple position-sinusoidal signals and identified the disturbance model parameters through spatial FFT. This model was applied to the feedforward compensation of RDC to effectively suppress position-dependent periodic disturbances.

Positional motion control experiments were conducted on a PMSM test bench to compare the suppression capabilities of two spatial domain control designs (SILC and SRC) and the RDC design across different motion velocities. The comparison also included the impact of each control design on the PMSM position-tracking performance, specifically focusing on transient-state and steady-state errors. The experimental results indicate that while both SILC and SRC effectively suppress position-dependent periodic disturbances, SILC exhibits a slower convergence of position errors owing to its learning process. Moreover, as the PMSM motion velocity increases, both SILC and SRC significantly increase the position error. Compared with the two spatial domain control designs, RDC rapidly suppresses position-dependent periodic disturbances and reduces position error, making it less susceptible to changes in the PMSM motion velocity. The position error reduction rate can reach 90%. These results validated the feasibility and superior performance of the RDC developed in this study.

Author Contributions: Conceptualization, S.-S.Y. and Z.-H.L.; Data curation, S.-S.Y. and Z.-H.L.; Formal analysis, S.-S.Y. and Z.-H.L.; Funding acquisition, S.-S.Y.; Investigation, S.-S.Y. and Z.-H.L.; Methodology, S.-S.Y. and Z.-H.L.; Project administration, S.-S.Y.; Resources, S.-S.Y.; Software, Z.-H.L.; Supervision, S.-S.Y.; Validation, S.-S.Y. and Z.-H.L.; Visualization, S.-S.Y. and Z.-H.L.; Writing—original draft, S.-S.Y. and Z.-H.L.; Writing—review and editing, S.-S.Y. All authors have read and agreed to the published version of the manuscript.

Funding: This research was funded in part by the National Science and Technology Council, Taiwan, grant number MOST108-2622-E-007-015-CC2 and NSTC113-2221-E-027-073.

Data Availability Statement: Data are contained within the article.

Acknowledgments: The authors would like to thank Chen-Chou Hsieh (Shihlin Electric & Engineering Corp., Taiwan) for his valuable comments on the design of PMSM servo drives.

Conflicts of Interest: The authors declare no conflicts of interest.

References

1. Mooren, N.; Witvoet, G.; Oomen, T. Gaussian process repetitive control with application to an industrial substrate carrier system with spatial disturbances. *IEEE Trans. Control. Syst. Technol.* **2023**, *31*, 344–358. [CrossRef]
2. Liu, Q.; Huo, X.; Liu, K.Z.; Zhao, H. Accurate cycle aligned repetitive control for the rejection of spatially cyclic disturbances. *IEEE Trans. Ind. Electron.* **2022**, *69*, 6173–6181. [CrossRef]
3. Huo, X.; Wang, M.; Liu, K.Z.; Tong, X. Attenuation of position-dependent periodic disturbance for rotary machines by improved spatial repetitive control with frequency alignment. *IEEE/ASME Trans. Mechatron.* **2020**, *25*, 339–348. [CrossRef]
4. Rafaq, M.S.; Midgley, W.; Steffen, T. A review of the state of the art of torque ripple minimization techniques for permanent magnet synchronous motors. *IEEE Trans. Ind. Inform.* **2023**, *20*, 1019–1031. [CrossRef]
5. Yeh, S.S.; Hong, M.J. Proportional-integral-proportional control and compensation design for low-speed motions of permanent magnet synchronous motor driven servomechanism with position-dependent disturbance. *J. Chin. Inst. Eng. Trans. Chin. Inst. Eng. Ser. A* **2022**, *45*, 602–612. [CrossRef]
6. Chen, Y.; Zhang, S.; Zhang, Y.; Lu, Z.; Zhao, C. Investigation on sensorless estimating method and characteristics of friction for ball screw system. *Appl. Sci.* **2020**, *10*, 3122. [CrossRef]
7. Zhou, Z.; Wang, H. Full life-cycle cutting force prediction in ball helical milling based on oblique cutting analysis. *Int. J. Adv. Manuf. Technol.* **2023**, *124*, 1623–1638. [CrossRef]
8. Yeh, S.S.; Jiang, W.J. Development of pitch cycle-based iterative learning contour control for thread milling operations in CNC machine tools. *Appl. Sci.* **2023**, *13*, 6447. [CrossRef]
9. Wang, H.; Wang, J.; Zhang, J.; Tao, K.; Wu, D. Identification and analysis of cutting force coefficients in the helical milling process. *J. Adv. Mech. Des. Syst. Manuf.* **2020**, *14*, JAMDSM0020. [CrossRef]
10. Ciulli, E.; Fazzolari, F.; Pugliese, G. Contact force measurements in cam and follower lubricated contacts. *Front. Mech. Eng.* **2020**, *6*, 601410. [CrossRef]
11. Wang, X.; Wang, X.; Wang, Z.; Xiao, X.; Li, S. Composite finite-time control for PMSM with prescribed performance using disturbance compensation technique. *Control Eng. Pract.* **2023**, *141*, 105677. [CrossRef]
12. Huang, Z.; Chen, M.; Lungu, M. Interconnected disturbance observer-based tracking control for permanent magnet synchronous motors. *IEEE Trans. Control. Syst. Technol.* **2023**, *31*, 2953–2960. [CrossRef]
13. Hu, M.; Hua, W.; Wang, Z.; Li, S.; Wang, P.; Wang, Y. Selective periodic disturbance elimination using extended harmonic state observer for smooth speed control in PMSM drives. *IEEE Trans. Power Electron.* **2022**, *37*, 13288–13298. [CrossRef]
14. Duan, J.; Wang, S.; Sun, L. Backstepping sliding mode control of a permanent magnet synchronous motor based on a nonlinear disturbance observer. *Appl. Sci.* **2022**, *12*, 11225. [CrossRef]
15. Liu, Y.C.; Laghrouche, S.; Depernet, D.; Djerdir, A.; Cirrincione, M. Disturbance-observer-based complementary sliding-mode speed control for PMSM drives: A super-twisting sliding-mode observer-based approach. *IEEE J. Emerg. Sel. Top. Power Electron.* **2021**, *9*, 5416–5428. [CrossRef]
16. Liu, J.; Li, H.; Deng, Y. Torque ripple minimization of PMSM based on robust ILC via adaptive sliding mode control. *IEEE Trans. Power Electron.* **2018**, *33*, 3655–3671. [CrossRef]
17. Huo, X.; Wu, A.; Wang, R.; Ma, K. Data-driven iterative tuning for rejecting spatial periodic disturbances combined with LESO. *IFAC-PapersOnLine* **2020**, *53*, 3959–3964. [CrossRef]
18. Mohammed, S.A.Q.; Nguyen, A.T.; Choi, H.H.; Jung, J.W. Improved iterative learning control strategy for surface-mounted permanent magnet synchronous motor drives. *IEEE Trans. Ind. Electron.* **2020**, *67*, 10134–10144. [CrossRef]
19. Lei, J.; Fang, S.; Huang, D.; Wang, Y. Enhanced deadbeat predictive current control for PMSM drives using iterative sliding mode observer. *IEEE Trans. Power Electron.* **2023**, *38*, 13866–13876. [CrossRef]
20. Wang, J.; Huang, D.; Fang, S.; Wang, Y.; Xu, W. Model predictive control for arc motors using extended state observer and iterative learning methods. *IEEE Trans. Energy Convers.* **2022**, *37*, 2217–2226. [CrossRef]
21. Hara, S.; Yamamoto, Y.; Omata, T.; Nakano, M. Repetitive control system: A new type servo system for periodic exogenous signals. *IEEE Trans. Autom. Control.* **1988**, *33*, 659–668. [CrossRef]
22. Tomizuka, M.; Tsao, T.C.; Chew, K.K. Discrete-time domain analysis and synthesis of repetitive controllers. In Proceedings of the 1988 American Control Conference, Atlanta, GA, USA, 15–17 June 1988; pp. 860–866. [CrossRef]
23. Mahawan, B.; Luo, Z.H. Repetitive control of tracking systems with time-varying periodic references. *Int. J. Control.* **2000**, *73*, 1–10. [CrossRef]
24. Steinbuch, M. Repetitive control for systems with uncertain period-time. *Automatica* **2002**, *38*, 2103–2109. [CrossRef]

25. Steinbuch, M.; Weiland, S.; Singh, T. Design of noise and period-time robust high-order repetitive control, with application to optical storage. *Automatica* **2007**, *43*, 2086–2095. [CrossRef]
26. Kalyanam, K.; Tsao, T.C. Two-period repetitive and adaptive control for repeatable and nonrepeatable runout compensation in disk drive track following. *IEEE/ASME Trans. Mechatron.* **2012**, *17*, 756–766. [CrossRef]
27. Cui, P.; Wang, Q.; Zhang, G.; Gao, Q. Hybrid fractional repetitive control for magnetically suspended rotor systems. *IEEE Trans. Ind. Electron.* **2018**, *65*, 3491–3498. [CrossRef]
28. Blanken, L.; Bevers, P.; Koekebakker, S.; Oomen, T. Sequential multiperiod repetitive control design with application to industrial wide-format printing. *IEEE/ASME Trans. Mechatron.* **2020**, *25*, 770–778. [CrossRef]
29. Broberg, H.L.; Molyet, R.G. A new approach to phase cancellation in repetitive control. In Proceedings of the 1994 IEEE Industry Applications Society Annual Meeting, Denver, CO, USA, 2–6 October 1994; pp. 1766–1770. [CrossRef]
30. Wu, C.J.; Tsai, M.C.; Cheng, L.J. Design and implementation of position-based repetitive control torque observer for cogging torque compensation in PMSM. *Appl. Sci.* **2020**, *10*, 96. [CrossRef]
31. Castro, R.S.; Flores, J.V.; Salton, A.T. Robust discrete-time spatial repetitive controller. *IEEE Trans. Control. Syst. Technol.* **2019**, *27*, 2696–2702. [CrossRef]
32. Yeh, S.S.; Su, H.C. Development of friction identification methods for feed drives of CNC machine tools. *Int. J. Adv. Manuf. Technol.* **2011**, *52*, 263–278. [CrossRef]
33. Yeh, S.S.; Chang, Y.C. Development of an extended proportional–integral–proportional control for improving positional motion performance of permanent magnet synchronous motor-driven servomechanism. *Asian J. Control.* **2022**, *24*, 2969–2980. [CrossRef]
34. Xia, X.; Zhang, B.; Li, X. High precision low-speed control for permanent magnet synchronous motor. *Sensors* **2020**, *20*, 1526. [CrossRef] [PubMed]
35. Yao, W.S.; Tsai, M.C.; Yamamoto, Y. Implementation of repetitive controller for rejection of position-based periodic disturbances. *Control. Eng. Pract.* **2013**, *21*, 1226–1237. [CrossRef]